The key role of bismuth in the magnetoelastic transitions of $Ba_3BiIr_2O_9$ and $Ba_3BiRu_2O_9$ as revealed by chemical doping

Peter E.R. Blanchard[†], Zixin Huang[†], Brendan J. Kennedy[†], Samuel Liu[†], Wojciech Miiller[†,§], Emily Reynolds[†], Qingdi Zhou[†], Maxim Avdeev[§], Zhaoming Zhang[§], Jade B. Aitken[¶], Bruce C.C. Cowie[^], Ling-Yun Jang[≠], Thiam Teck Tan[≈], Sean Li[≈], and Chris D. Ling[†*]

[†]*School of Chemistry, The University of Sydney, Sydney, NSW 2006 Australia*

[§]*Australian Nuclear Science and Technology Organisation, Lucas Heights, New South Wales, 2234, Australia*

[¶]*Institute of Materials Structure Science, KEK, Tsukuba, Ibaraki, 305-0801, Japan*

[^]*Australian Synchrotron, 800 Blackburn Road, Clayton, Victoria 3168, Australia*

[≠]*Facility Utilization Group, Experiment Facility Division, National Synchrotron Radiation Research Center, Hsinchu 30076, Taiwan*

[≈]*School of Materials Science and Engineering, University of New South Wales, NSW 2052, Australia*

Abstract

The key role played by bismuth in an average intermediate oxidation state in the magnetoelastic spin-gap compounds $Ba_3BiRu_2O_9$ and $Ba_3BiIr_2O_9$ has been confirmed by systematically replacing bismuth with La^{3+} and Ce^{4+}. Through a combination of powder diffraction (neutron and synchrotron), X-ray absorption spectroscopy, and magnetic properties measurements, we show that Ru/Ir cations in $Ba_3BiRu_2O_9$ and $Ba_3BiIr_2O_9$ have oxidation states between +4 and +4.5, suggesting that Bi cations exist in an unusual average oxidation state intermediate between the conventional +3 and +5 states (which is confirmed by the Bi L_3-edge spectrum of $Ba_3BiRu_2O_9$). Precise measurements of lattice parameters from synchrotron diffraction are consistent with the presence of intermediate oxidation state bismuth cations throughout the doping ranges. We find that relatively small amounts of doping (~10 at%) on the bismuth site suppress and then completely eliminate the sharp structural and magnetic transitions observed in pure $Ba_3BiRu_2O_9$ and $Ba_3BiIr_2O_9$, strongly suggesting that the unstable electronic state of bismuth plays a critical role in the behaviour of these materials.

Introduction

In recent years, there has been a great deal of interest in systems that exhibit quantum cooperative phenomena due to coupling between magnetic, electronic, and orbital degrees of freedom.[1] A number of low-dimensional antiferromagnetic (AFM) dimer systems exhibit quantum cooperative phenomena where the interactions between neighbouring electronic spin result in a gap opening between the singlet ground state and the excited triplet state,[2] such as $TlCuCl_3$,[3] $Ba_3Cr_2O_8$,[4] and $CuIr_2S_4$.[5] We recently observed spin-gap AFM in $Ba_3BiRu_2O_9$ and $Ba_3BiIr_2O_9$ at T^* = 176 K and 74 K, respectively.[6,7] Interestingly, both of these phases exhibit magnetoelasticity, with a negative thermal volume expansion occurring in response to the spin-gap opening. Such magnetoelastic effects are rare and, pointedly, were not observed for any other members of the isostructural series of compounds $Ba_3\mathit{Ln}Ru_2O_9$ and $Ba_3\mathit{Ln}Ir_2O_9$ (where *Ln* = lanthanoid).[8-11] This suggests that Bi atoms play a crucial role in their unique properties.

$Ba_3BiRu_2O_9$ and $Ba_3BiIr_2O_9$ belong to the 6H-peroviskes $A_3BM_2O_9$ family of oxides. At room temperature, they both crystallize in a monoclinically distorted structure (space group $C2/c$) derived from the parent high-temperature hexagonal structure (space group $P6_3/mmc$).[12,13] The same monoclinic distortion is observed in, for example, $Ba_3LaIr_2O_9$ and $Ba_3NdIr_2O_9$.[11] 6H-perovskites contain face-sharing bi-octahedral M_2O_6 dimers that share vertices with BiO_6 octahedra, with high-coordinate Ba^{2+} cations on the *A* site. *M*-*M* bonding within the M_2O_6 dimers results in a small trigonal distortion along the *c*-direction. *M*-*M* bond distances are relatively short at ~2.5 Å, allowing for the possibility of direct metal-metal bonding.[12,13] The oxidation states of *M* and *B* are coupled, with $B^{3+}/M^{4.5+}$ and B^{4+}/M^{4+} the most common combination (B^{4+}/M^{4+} typically has the smaller unit cell). The unit cell volumes of $Ba_3BiRu_2O_9$ and $Ba_3BiIr_2O_9$ are comparable to those of other B^{4+}/M^{4+} 6H perovskites, suggesting that the oxidation state of Bi is +4.

Bi^{4+} cations would have unstable [Xe]$4f^{14}5d^{10}6s^1$ electronic configurations, and have never been observed in solid-state oxides. Bi in a nominal oxidation state of +4 is expected to undergo charge disproportionation to a mixture of Bi^{3+} and Bi^{5+}, as shown in neutron diffraction and extended X-ray absorption fine-structure (EXAFS) studies of $BaBiO_3$.[15-19] X-ray absorption near-edge spectroscopy (XANES) indicates minimal charge transfer between the two Bi sites in $BaBiO_3$,[20,21] although conflicting results have been obtained from X-ray photoelectron spectroscopy (XPS).[21-23] Differences between the two methods may reflect the sensitivity of Bi 4f XPS analysis to surface adsorbates and Ar^+ ion beam reduction. Whilst XPS and XANES are widely used to determine effective oxidation states, recent studies have suggested that these techniques may be equally sensitive to local structure and bonding effects.[24,25]

For $Ba_3BiRu_2O_9$ and $Ba_3BiIr_2O_9$, we could find no evidence for Bi^{3+}/Bi^{5+} disproportionation in our detailed high-resolution neutron and synchrotron X-ray diffraction studies, the structure rigidly adhering to $C2/c$ space group symmetry with only one unique Bi (and one unique Ir) site both above and below the magnetoelastic spin-gap transitions at T^*.[6,7] We also saw no evidence in peak shapes or anisotropic atomic displacement parameters for local disproportionation, noting that the BiO_6 octahedra are distributed on a pseudo-hexagonal lattice that could frustrate long-range ordering; or for charge transfer from Bi to M (*i.e.*, $Bi^{4+}/M^{4+} \rightarrow Bi^{3+}/M^{4.5+}$). Either of these could potentially also have provided an explanation for the observed negative thermal volume expansion at T^*. The true oxidation state of Bi in these phases is therefore worthy of further investigation.

While we cannot directly test for the presence of Bi^{4+}, due to the absence of any other examples for comparison, we can make indirect inferences based on its electronic effects on other metal atoms in the 6H perovskites. In the work reported here, we have approached this by substituting lanthanoid cations of similar size and unambiguous valence state (*i.e.*, La^{3+} and Ce^{4+}) for Bi and monitoring the effects on the valence state and bonding environments of all B and M cations. We have used XANES, physical property measurements and powder diffraction (neutron and synchrotron X-ray) measurements to study the structural and electronic properties of $Ba_3Ce_{1-x}Bi_xRu_2O_9$, $Ba_3La_{1-x}Bi_xRu_2O_9$, and $Ba_3La_{1-x}Bi_xIr_2O_9$. $Ba_3La_{1-x}Ce_xRu_2O_9$ was also analyzed for comparison purposes. Our previous Ru/Ir L_3-edge XANES studies have shown that these edges are well-defined and extremely sensitive to the oxidation states of Ru/Ir.[7,26] Our results confirm that the average oxidation state of Bi is intermediate between +3 and +5 in $Ba_3BiRu_2O_9$ and $Ba_3BiIr_2O_9$, and that there is no evidence for long-range-ordered charge disproportionation into those conventional states.

Experimental

Polycrystalline (powder) samples of $Ba_3La_{1-x}Ce_xRu_2O_9$, $Ba_3Ce_{1-x}Bi_xRu_2O_9$, $Ba_3La_{1-x}Bi_xRu_2O_9$ and $Ba_3La_{1-x}Bi_xIr_2O_9$ ($0 \leq x \leq 1$) were prepared using the methods described previously for $Ba_3BiIr_2O_9$ and $Ba_3BiRu_2O_9$.[12,13] All samples were prepared from stoichiometric amounts of $BaCO_3$, Bi_2O_3, La_2O_3, CeO_2, Ru metal and Ir metal reacted at high temperatures in air. Starting materials were obtained from commercial suppliers with purities greater than 99.98%. $BaCO_3$, La_2O_3, and CeO_2 were dried at 1000 K overnight before use. Reaction progress was monitored using a Panalytical X'Pert X-ray diffractometer (XRD) equipped with a Cu Kα X-ray source. Variable-temperature neutron powder diffraction (NPD) data were collected on the high-resolution instrument Echidna at the OPAL reactor (ANSTO, Lucas Heights, Australia) between 3 and 300 K using a closed-cycle helium cryostat over the angular range $10 \leq 2\theta \leq 160°$ with a neutron wavelength of $\lambda = 2.4395$ Å,[27] obtained using a Ge (331) monochromator. Samples were placed in 6 mm diameter vanadium cans.

Variable-temperature synchrotron XRD (S-XRD) data were collected at the Powder Diffraction beamline of the Australian Synchrotron (Melbourne, Australia) between 100 and 300 K over angular range of $5 \leq 2\theta \leq 85°$ with a X-ray wavelength of 0.82460 Å (calibrated against a LaB_6 standard).[28] Finely ground samples were placed in unsealed 0.3 mm diameter quartz capillaries, which were cooled with a liquid nitrogen cryostream. The sample was rotated during the measurements.

Rietveld-refinements against NPD and S-XRD data were carried out using the GSAS[29] program with the EXPGUI[30] front-end. The structural models used were those previously reported for pure $Ba_3BiIr_2O_9$ and $Ba_3BiRu_2O_9$.[4,5] Scale factors, zero-shifts, background functions, and single Lorentzian broadening terms on top of the standard pseudo-Voigt peak shape functions for the instruments were refined in addition to the unit cell parameters. Atomic displacement parameters (ADPs) were constrained to be equal for atoms of the same species.

DC magnetic susceptibility data were measured using a Quantum Design Physical Properties Measurement System (PPMS). Data were collected from 300 to 2 K in a field of 10000 Oe using the vibrating sample magnetometer (VSM) technique.

Ru L_3-edge and Ce $M_{5,4}$-edge XANES spectra were collected on the Soft X-ray beamline at the Australian Synchrotron.[31] Powder samples were thinly dusted onto double-sided carbon tape (SPI Supplies) and inserted into the vacuum chamber *via* a load lock. The pressure inside the analysis chamber was maintained at better than ~10^{-9} torr. Spectra were collected from ~30 eV below to ~100 eV above the edge using both fluorescence and total electron yield (TEY) mode. All spectra were taken simultaneously with a TEY signal measured from a standard $Ru(OH)Cl_3$ reference foil in the beamline. This reference foil removed approximately 10% of the beam intensity. The peak height of the Ru L_3-edge XANES spectra of $Ru(OH)Cl_3$ was set to 2840.1 eV. ($Ru(OH)Cl_3$ was itself calibrated against Ru metal with the maximum of the first derivate set to 2838 eV.) The Ce $M_{5,4}$-edge was calibrated against Ce metal with the maximum of the first derivative of the M_5-edge set to 883.8 eV.

Additional Ru L_3-edge and Ce L_3-edge XANES spectra were collected on beamline 16A1 at the National Synchrotron Radiation Research Center (NSRRC) in Hsinchu, Taiwan.[32] Finely ground samples were dispersed onto Kapton tape and placed in the X-ray beam at a 45° angle. Spectra were collected from ~50 eV below to ~200 eV in fluorescence yield mode using a Lytle detector. An energy step-size of 0.2 eV was used near the absorption edge. The Ce L_3-edge spectra were calibrated against elemental Cr with the maximum in the first derivative of the K-edge set to 5989.2 eV. Ru L_3-edge XANES spectra were calibrated against elemental Mo with the maximum of the first derivative of the L_2-edge set to 2625 eV.

Ir and Bi L_3-edge XANES spectra were collected on Beamline 20B at the Photon Factory in Tsukuba, Japan.[33] Powder samples were sandwiched between Kapton tape and positioned in the X-ray beam at a 45° angle. Spectra were collected from ~50 eV below to ~200 eV above the edge in fluorescence mode with a step size of 0.5 eV and a dwell time of 1s. X-rays were monochromated using a Si(111) monochromator, which was detuned by 50% to reject higher harmonics. The Ir L_3-edge was calibrated against elemental Ge with the maximum of the first derivative of the Ge K-edge set to 11103 eV. The Bi L_3-edge was calibrated against elemental Au with the maximum of the first derivative of the Au L_2-edge set to 13734 eV; these data were collected for $Ba_3BiIr_2O_9$ but could not be collected for $Ba_3BiIr_2O_9$ due to the overlap of the Bi L_3-edge with the Ir L_1-edge.

All XANES data were analyzed using the Athena software package.[34] Additional peak fitting analysis was performed using the CasaXPS software package.[35]

Results and Discussion

Diffraction studies

As shown in Figure 1, Rietveld-refinements against room-temperature S-XRD data yield linear (Vegard's Law) changes in unit cell volume due to *B*-site doping across all solid solutions. The value for the pure Ce phase $Ba_3CeRu_2O_9$ is taken from Doi *et al.*[10] Figure 1 also illustrates the variation in the unit cell angle β, which shows second-order behaviour in evolving from the monoclinic *B* = Bi phases to the hexagonal *B* = La, Ce phases.

The unit cell volume changes across these solid solutions can be directly related to changes in the effective ionic radii (IR) of the various 6-fold coordinate *B*-site cations.[36] The IR of La^{3+} and Bi^{3+} are both 1.03 Å, so the experimentally observed decreases in volume with increasing x in the series $Ba_3La_{1-x}Bi_xRu_2O_9$ and $Ba_3La_{1-x}Bi_xIr_2O_9$ (Figure 1) are direct evidence for an oxidation state of Bi higher that +3 in these phases. The Vegard's Law behaviour of the solid solutions (Figure 1) can be used to estimate the oxidation state of Bi in $Ba_3BiRu_2O_9$ by direct comparison of its unit cell volume to those of $Ba_3CeRu_2O_9$ and $Ba_3LaRu_2O_9$, and similarly for $Ba_3BiIr_2O_9$, and interpolating between the IR for Bi^{3+} (1.03 Å) and Bi^{5+} (0.76 Å). This yields effective oxidation states of +3.53 for $Ba_3BiRu_2O_9$ and +3.44 for $Ba_3BiIr_2O_9$. These values are only approximate, because there is not necessarily a linear relationship between oxidation state and IR; however, that relationship is always at least monotonic.

Rietveld-refinement of unit cell volumes at the Bi-rich end of the $Ba_3La_xBi_{1-x}Ir_2O_9$ and $Ba_3La_xBi_{1-x}Ru_2O_9$ solid solutions (using NPD and S-XRD data respectively) show suppression and then elimination of the negative thermal volume expansion associated with the AFM ordering temperature (T*) as La is doped for Bi (Figure 2). The transition in the Ru compounds has a smaller effect on the structure, but is observed to be considerably more robust to doping than in the Ir compounds, where 5% La is sufficient to completely suppress it. This is consistent with the fact that between the undoped Ru and Ir compounds, T* is significantly higher for the former than for the latter.

Magnetic susceptibility studies

Magnetic susceptibility data show suppression, and then elimination, of the AFM ordering temperature (T*) and associated spin-gap transition upon doping La or Ce for Bi (Figure 3). The trends are identical to those for the negative thermal volume expansion observed by diffraction, with the exception of $Ba_3La_xBi_{1-x}Ir_2O_9$, where susceptibility anomalies are seen at 50 K for x = 0.95 and at 7 K for x = 0.90 in Figure 3(a) but no corresponding volume expansion is seen in Figure 2(a). This can be explained by T* being considerably lower in the iridates compared to the ruthenates, so that less thermal energy is available to distort the crystal structure upon magnetic ordering, decoupling the magnetoelastic effect in these samples.

XANES analysis

Trends in the lattice parameters of the solid solutions suggest that Bi cations have an oxidation state greater than +3. However, the stereochemically active $6s^2$ lone pair on Bi^{3+} often has an influence on structure and properties,[37] and its possible effects should be considered. [Note further that this lone pair would still be partially occupied for any hypothetical oxidation state below +5.] Despite the absence of any evidence for long-range symmetry lowering distortions in our compounds, displacive disorder due to $6s^2$ lone pairs might cause only local structural deviations, similar to those observed in pyrochlores $Bi_2Ru_2O_7$ [38] and Bi_2InNbO_7.[39] Displacive disorder can in turn have an impact on magnetic properties, as observed in $BiMnO_3$ and

$BiFeO_3$.[40] In order to confirm that the structural and magnetic property trends described above are not due to displacive disorder, XANES analysis was performed on all solid solutions.

Attempts were made to directly probe the oxidation state of Bi in $Ba_3BiRu_2O_9$ by analyzing the Bi L_3-edge XANES spectrum (Figure 4). There are distinct line-shape differences between Bi_2O_3 (Bi^{3+} reference) and Ba_2LuBiO_6 (Bi^{5+} reference), notably a low energy peak corresponding to a 2p-to-6s transition that is only observed in Bi^{5+} systems,[41] while the line-shape for our "Bi^{4+}" (disproportionated Bi^{3+}/Bi^{5+}) reference, $BaBiO_3$, is intermediate between the two. The Bi L_3-edge of $Ba_3BiRu_2O_9$ is clearly most similar to $BaBiO_3$, confirming an intermediate oxidation state for Bi. It should be noted that these data cannot distinguish between a discrete "Bi^{4+}" state and a dispropotionated Bi^{3+}/Bi^{5+} state. However, when combined with our previous high-resolution diffraction studies that showed no evidence for any long-range symmetry lowering (either above or below T^*) from the $C2/c$ structure with one crystallographically unique Bi site,[6,7] they do provide clear evidence for unconventional oxidation state behaviour of Bi in these compounds.

The Ru L_3-edge XANES spectra of $Ba_3BRu_2O_9$ (B = La, Ce, Bi) are shown in Figure 5a, along with the spectra obtained from the $SrRuO_3$ (Ru^{4+}) and Sr_2YRuO_6 (Ru^{5+}) standards in Figure 5b. The Ru L_3-edge corresponds to the dipole-allowed transition of a $2p_{3/2}$ electron into unoccupied 4d states. Two features are observed in all Ru L_3-edge XANES spectra, corresponding to the t_{2g} (low energy) and e_g (high energy) states in 6-coordinate octahedral systems.[42,43] Because these states are directly involved in Ru-O bonding, information on the oxidation state of Ru can be obtained from the L_3-edge spectral shape and absorption edge energy. In general, absorption edge energy should increase with increasing oxidation state. This is best illustrated by the higher Ru L_3-edge absorption edge energy of $Ba_3LaRu_2O_9$ (2838.6 eV) compared to $Ba_3CeRu_2O_9$ (2838.1 eV). The difference in energy is small (0.5 eV), noting that the absorption energy difference between $SrRuO_3$ (Ru^{4+}) and Sr_2YRuO_6 (Ru^{5+}) is ~0.9 eV, as illustrated in Figures 5a and 5b. The e_g peak also shows a notable shift to high absorption energy with increasing oxidation state, consistent with an increase in crystal field splitting. Similar absorption energy differences were observed in fluorescence spectra (see Figure S1 in Supporting Information). Overall, our data are consistent with the presence of $Ru^{4.5+}$ in $Ba_3LaRu_2O_9$ and Ru^{4+} in

$Ba_3CeRu_2O_9$. Surprisingly, the absorption edge energy of $Ba_3BiRu_2O_9$ (2838.5 eV) is similar to that of $Ba_3LaRu_2O_9$. Based on our previous XANES analysis on $Ba_3\mathit{B}Ir_2O_9$,[7] we had anticipated $Ba_3BiRu_2O_9$ would be more similar to $Ba_3CeRu_2O_9$ (*i.e.*, Ru^{4+}/Bi^{4+}).

Representative Ru L_3-edge XANES spectra of the $Ba_3La_{1-x}Ce_xRu_2O_9$, $Ba_3La_{1-x}Bi_xRu_2O_9$ and $Ba_3Ce_{1-x}Bi_xRu_2O_9$ series are shown in Figure 6. Generally, the Ru L_3-edge absorption edge energy of the solid solutions is between those of the parent $Ba_3\mathit{B}Ru_2O_9$ (Figure 7). As expected, $Ba_3La_{1-x}Ce_xRu_2O_9$ shows a gradual decrease in absorption edge energy across the series, as well as a shift in the e_g peak to lower absorption energy, consistent with a gradual decrease in the oxidation state of Ru. Surprisingly, the same trend is not observed in $Ba_3La_{1-x}Bi_xRu_2O_9$. Although there is a small shift in the e_g peak to lower energy across the $Ba_3La_{1-x}Bi_xRu_2O_9$ series, there is little change in the absorption edge energy, suggesting only a very small change in the oxidation state of Ru. Significant increases in absorption edge energy are observed in $Ba_3Ce_{1-x}Bi_xRu_2O_9$, indicating an overall increase in the oxidation state of Ru across the series (as demonstrated below, Ce is present as Ce^{4+} throughout this series). The compositional dependency of the Ru oxidation state was confirmed from a linear combination fitting analysis using $Ba_3CeRu_2O_9$ (+4) and $Ba_3LaRu_2O_9$ (+4.5) as standards (Figure 8). It was estimated from this analysis that Ru in $Ba_3BiRu_2O_9$ has an oxidation states of +4.33, corresponding to an average oxidation state for Bi of +3.34. [Note that the reduced valence state of Ru could theoretically be explained by the presence of ~2% oxygen vacancies in the lattice; however, the fact that the Bi L_3-edge XANES spectra clearly show an intermediate oxidation state for Bi speaks against this interpretation.]

Our previously published Ir L_3-edge XANES analysis of $Ba_3BiIr_2O_9$ suggested that the Bi oxidation state was closer to +4 than +3.[7] To complement our current study of the $Ba_3La_{1-x}Bi_xRu_2O_9$ series, we collected and analyzed further Ir L_3-edge XANES spectra of several compounds in the $Ba_3La_{1-x}Bi_xIr_2O_9$ series (Figure 9). Like the Ru L_3-edge, the Ir L_3-edge XANES corresponds to a dipole-allowed transition of a $2p_{3/2}$ electron into unoccupied 5d states. The Ir L_3-edge is generally broader than the Ru L_3-edge, most likely as a consequence of the shorter core-hole lifetime.[44] The higher absorption edge energy of $Ba_3LaIr_2O_9$ (11216.3 eV) compared to $Ba_3BiIr_2O_9$ (11216.0 eV) is consistent with the presence of Ir^{4+} in $Ba_3BiIr_2O_9$.[7,45,46]

A gradual decrease in the intensity of the Ir L_3-edge is observed across the $Ba_3La_{1-x}Bi_xIr_2O_9$ series, indicating a gradual decrease in the oxidation state of Ir. This trend supports an average oxidation state for Bi close to +4 in $Ba_3BiIr_2O_9$. Attempts to verify this *via* a linear combination fitting analysis were unsuccessful as a consequence of the broad lineshape of the Ir L_3-edge.

Ce L_3-edge XANES spectra were analyzed to determine whether doping affects the oxidation state of the Ce atoms across the $Ba_3La_{1-x}Ce_xRu_2O_9$ and $Ba_3Ce_{1-x}Bi_xRu_2O_9$ series (Figure 10). The Ce L_3-edge is generally sensitive to the oxidation state of Ce, as evident from the comparison of the spectra for $Ce_{1/3}TaO_3$ (Ce^{3+}) and CeO_2 (Ce^{4+}).[47,48] Three features (labelled A-C) are observed in the Ce^{4+} species compared to the single broad whiteline observed in Ce^{3+} species. Features A, B, and C are believed to originate from the $4f^0$, $4f^1\underline{L}^1$, and $4f^2\underline{L}^2$ final states of Ce ($\underline{L}$ denotes a ligand hole), respectively.[49,50] Some authors have suggested that Peak C is characteristic of the presence of Ce^{3+} impurities.[51,52] The lineshape of the Ce L_3-edge XANES spectra of both the $Ba_3La_{1-x}Ce_xRu_2O_9$ and $Ba_3Ce_{1-x}Bi_xRu_2O_9$ series are similar to that of CeO_2, confirming the presence of Ce^{4+} throughout. Interestingly, the relative intensities and energy positions of peaks A-C in the ruthanates are different to those of CeO_2. In particular, peaks B and C are closer in energy in CeO_2. Although the difference in the lineshape may be due to the presence of Ce^{3+}, the lineshape of the ruthenates are similar to that observed for $BaCeO_3$, which was confirmed to contain no Ce^{3+} impurities.[53] The lineshape of the 6H perovskites may reflect differences in covalency and local coordination environment compared to CeO_2. Regardless, as evident in Figures 10b and 10c, there is no change in the lineshape of the Ce L_3-edge across both the $Ba_3La_{1-x}Ce_xRu_2O_9$ and $Ba_3Ce_{1-x}Bi_xRu_2O_9$ series, indicating no change in the oxidation state of Ce.

Further confirmation of the oxidation state of Ce was obtained by analyzing the Ce $M_{5,4}$-edge XANES spectra (Figure 11). The Ce $M_{5,4}$-edge corresponds to a dipole-allowed transition of the 3d electron into unoccupied 4f states. The M-edge is split by spin-orbit coupling into a lower-energy M_5-edge ($3d_{5/2}$ initial state) and a high-energy M_4-edge ($3d_{3/2}$ initial state). Figure 11 demonstrates that the lineshape of the Ce $M_{5,4}$-edge is very sensitive to the oxidation state of Ce.[54-57] The final state of Ce^{3+} ($4f^1$ final state) is vastly different than the final state of Ce^{4+} ($4f^0$ final state). As shown in Figure 11a, the Ce $M_{5,4}$-edge of $Ce_{1/3}TaO_3$ has five main features that are distinctly different from the four main features in CeO_2. These features are commonly used to identify the presence of Ce^{3+} and Ce^{4+}. In general, the Ce $M_{5,4}$-edge lineshapes in both the $Ba_3La_{1-x}Ce_xRu_2O_9$ and $Ba_3Ce_{1-x}Bi_xRu_2O_9$ series are similar to those in CeO_2, confirming the presence of Ce^{4+}. The lineshape of the fluorescence spectra (see Figure S2 in Supporting Information) all show features consistent with the presence of Ce^{4+}.

Conclusion

Our results conclusively demonstrate that Bi in $Ba_3BiIr_2O_9$ and $Ba_3BiRu_2O_9$ does not exist purely in conventional Bi^{3+} or Bi^{5+} states, but instead as either a disordered mixture of the two, or an unconventional intermediate state. Doping La^{3+} and Ce^{4+} for Bi results in lattice parameter changes consistent with Bi having an intermediate average oxidation state in these compounds. Bi L_3-edge XANES data confirm this. Ru L_3-edge XANES analysis of $Ba_3La_{1-x}Bi_xRu_2O_9$, $Ba_3Bi_{1-x}Ce_xRu_2O_9$, and $Ba_3La_{1-x}Ce_xRu_2O_9$ indicates that the Ru oxidation state in the undoped (pure Bi) phases is intermediate between +4 and +4.5, also implying a Bi oxidation state between +3 and +4 by charge balance. Importantly, the spectroscopic evidence means that the smaller unit cells relative to expectations for Bi^{3+} cannot be explained as an artefact of local displacive distortions driven by stereochemically active $6s^2$ lone pair on Bi^{3+}.

Such an intermediate oxidation state might normally be expected to lead to long-range ordered disproportionation into Bi^{3+} and Bi^{5+}, as for $BaBiO_3$. However, careful diffraction studies show that this does not occur in $Ba_3BiIr_2O_9$ or $Ba_3BiRu_2O_9$, most probably due to geometric frustration. This frustration is not resolved on cooling through the magnetoelastic transitions at T^*, with both compounds retaining $C2/c$ symmetry with one crystallographically unique Bi site down to at least 2 K. Our earlier temperature-dependent XANES measurements[6,7] also showed that Bi does not undergo any significant change down to, and through, the T^* transitions.

We believe that the unique presence of a magnetoelastic transition in $Ba_3BRu_2O_9$ and $Ba_3BIr_2O_9$ when B = Bi, but not when B is any lanthanoid (in +3 or +4 states) is related to the frustration of the unresolved average intermediate Bi oxidation state. A first-order transition producing such a large volume change (1.0% in the case of $Ba_3BiIr_2O_9$) could not normally occur at such a low temperature, and with virtually no hysteresis, because of the entropic barrier presented by the need for all M_2O_9 dimers in a crystallite to distort simultaneously. The inherent instability of Bi in these compounds could lower that barrier by acting as a charge and/or strain reservoir that destabilizes the structure, allowing the change in electronic configuration within the M_2O_9 dimers (the spin-gap opening) to produce the dramatic structural effects seen at T*.

Interestingly, we did not observe a T*-like magnetic and/or volume transition for any phase in the $Ba_3La_{1-x}Ce_xM_2O_9$ solid solutions; *i.e.*, an average intermediate oxidation state on the *B* site (and therefore on the *M* site) is not by itself sufficient to elicit the unusual low-temperature behaviour of $Ba_3BiRu_2O_9$ and $Ba_3BiIr_2O_9$. We are now embarking on the search for other transition metal oxides that could potentially contain Bi in "intermediate" oxidation states, to establish if $Ba_3BiRu_2O_9$ and $Ba_3BiIr_2O_9$ are unique, or the first examples of a broader class of materials with interesting low-temperature behaviour.

Acknowledgments

Work at the powder diffraction beamline at the Australian Synchrotron was performed with the assistance of Dr Helen Brand. Work performed at the NSRRC was supported by the Australian Synchrotron International Access Program. The High Energy Accelerator Research Organisation (KEK) in Tsukuba, Japan, provided operations support for the work at the Photon Factory. We acknowledge the support of the Australian Research Council – Discovery Projects (DP110102662).

Supporting Information

Supporting Information Available: Ru L_3-edge XANES spectra of $Ba_3BRu_2O_9$ (*B* = La, Ce, Bi) and the standards $SrRuO_3$ (Ru^{4+}) and Sr_2YRuO_6 (Ru^{5+}); representative Ce $M_{5,4}$-edge XANES spectra of $Ba_3La_{1-x}Ce_xRu_2O_9$ and $Ba_3Ce_{1-x}Bi_xRu_2O_9$. This material is available free of charge via the Internet at http://pubs.acs.org.

References

(1) Tokura, Y.; Nagaosa, N. *Science*, **2000**, *288*, 462-468.

(2) Vasil'ev, A. N.; Markina, M. M.; Popova, E. A. *Low. Temp. Phys.* **2005**, *31*, 272-299.

(3) Oosawa, A.; Ono, T.; Tanaka, H.; *Phys. Rev. B* **2002**, *66*, 020405.

(4) Nakajima, T.; Mitamura, H.; Ueda, Y.; *J. Phys. Soc. Japn.* **2006**, *75*, 054706.

(5) Radaelli, P. G.; Horibe, Y.; Gutmann, M. J.; Ishibashi, H.; Chen, C. H.; Ibberson, R. M.; Koyama, Y.; Hor, Y. S.; Kiryukhin, V.; Cheong, S. W.; *Nature*, **2002**, *416*, 155-158.

(6) Miiller, W.; Avdeev, M.; Zhou, Q.; Studer, A. J.; Kennedy, B. J.; Kearley, G. J.; Ling, C. D. *Phys. Rev. B*, **2011**, *84*, 220406(R).

(7) Miiller, W.; Avdeev, M.; Zhou, Q.; Kennedy, B. J.; Sharma, N.; Kutteh, R.; Kearley, G. J.; Schmid, S.; Knight, K. S.; Blanchard, P. E. R.; Ling, C. D.; *J. Am. Chem. Soc.* **2012**, *134*, 3265-3270.

(8) Doi, Y.; Hinatsu, Y. *J. Mater. Chem.* **2002**, *12*, 1792-1795.

(9) Hinatsu, Y.; Doi, Y. *Bull. Chem. Soc. Jpn.* **2003**, *76*, 1093-1113.

(10) Doi, Y.; Wakeshima, M.; Hinatsu, Y.; Tobo, A.; Ohoyama, K.; Yamaguchi, Y.; *J. Mater. Chem.* **2001**, *11*, 3135-3140.

(11) Y. Doi, Y. Hinatsu, *J. Phys.: Conden. Matter* **2004**, *16*, 2849-2860.

(12) J. Darriet, R. Bontchev, C. Dussarrat, F. Weill, B Darriet, *Eur. J. Solid State Inorg. Chem.* **1993**, *30*, 287-296.

(13) Ling, C. D.; Kennedy, B. J.; Zhou, Q.; Spencer, J. R.; Avdeev, M. *J. Solid State Chem.* **2010**, *183*, 727-735.

(14) Chailout, C.; Santoro, P.; Remeika, A.; Cooper, A. S.; Espinosa, G. P.; Marezio, M. *Solid State Commun.* **1988**, *65*, 1363-1369.

(15) Kennedy, B. J.; Howard, C. J.; Knight, K. S.; Zhang, Z.; Zhou, Q. *Acta Crystallogr. B.* **2006**, *62*, 537-546.

(16) Thornton, G.; Jacobson, A. J. *Acta Cryst. B* **1978**, *34*, 351-354.

(17) Zhou, Q.; Kennedy, B. J.; *Solid State Commun.* **2004**, *132*, 389-392.

(18) Balzarotti, A.; Menushenkov, A. P.; Motta, N.; Purans, J. *Solid State Commun.* **1984**, *49*, 887-890.

(19) Flavell, W. F.; Mian, M.; Roberts, A. J.; Howlett, J. F.; Sarker, M. M.; Wincott, P. L.; Bilsborrow, R. L.; Van Dorssen, G. *J. Mater. Chem.* **1997**, *7*, 357-364.

(20) Akhtar, Z. N.; Akhtar, M. J.; Catlow, C. R. A. *J. Phys.: Condens. Matter* **1993**, *5*, 2643-2646.

(21) Kulkarni, G. U.; Vijayakrishnan, V.; Rao, G. R.; Seshadri, R.; Rao, C. N. R. *Appl. Phys. Lett.* **1990**, *57*, 1823-1824.

(22) Nagoshi, M.; Suzukit, T.; Fukuda, Y.; Ueki, K.; Tokiwa, A.; Kikuchi, M.; Syono, Y.; Tachiki, M. *J. Phys.: Condens. Matter* **1992**, *4*, 5769-5781.

(23) Korolkov, D. V.; Kostikova, G. P.; Kostikov, Y. P. *Physica C* **2002**, *383*, 117-121.

(24) Quan, Z.; Hu, H.; Hu, S.; Liu, W. *J. Sol-Gel Sci. Technol.* **2008**, *48*, 261-266.

(25) Jiang, N.; Spence, J. C. H. *J. Phys.: Condens. Matter* **2006**, *18*, 8029-8036.

(26) Qasim, I.; Kennedy, B. J.; Zhang, Z.; Avdeev, M.; Jang, L. Y. *J. Phys.: Condens. Matter* **2011**, *23*, 435401.

(27) Liss, K. D.; Hunter, B.; Hagen, M.; Noakes T.; Kennedy, S. *Physica B* **2006**, *385-86*, 1010-1012.

(28) Wallwork, K. S.; Kennedy, B. J.; Wang, D. *AIP Conference Proceedings* **2007**, *879*, 879-882.

(29) Toby, B. H. *J. Appl. Cryst.* **2001**, *34*, 210-213

(30) Brese, N. E.; O'Keeffe, M. *Acta Cryst. B* **1991**, *47*, 192-197.

(31) Cowie, B. C. C.; Tadich, A.; Thomsen, L. *AIP Conf. Proc.* **210**, *1234*, 307-310.

(32) Dann, T. E.; Chung, S. C.; Huang, L. J.; Juang, J. M.; Chen C. I.; Tsang, K. L. *J. Synchrot. Radiat.* **1998**, *5*, 664-666.

(33) Sabine, T. M.; Kennedy, B. J.; Garrett, R. F.; Foran, G. J.; Cookson, D. J. *J. Appl. Crystallogr.* **1995**, *28*, 513-517.

(34) Ravel, B.; Newville, M. *J. Synchrotron Rad.* **2005**, *12*, 537-541.

(35) Fairley, N. *CasaXPS*, version 2.3.17dev5.9n; Casa Software, Ltd.: Teignmouth, Devon, U.K., 2012 (www.casaxps.com).

(36) Shannon, R. D. *Acta Cryst.* **1976**, *A32*, 751-767.

(37) Stoltzfus, M. W.; Woodward, P. M.; Seshadri, R.; Klepeis, J. H.; Bursten, B. *Inorg. Chem.* **2007**, *46*, 3839-3850.

(38) Avdeev, M.; Haas, M. K.; Jorgensen, J. D.; Cava, R. J. *J. Solid State Chem.* **2002**, *169*, 24-34

(39) Zhou, Q.; Kennedy, B. J.; Ting, V.; Withers, R. L. *J. Solid State Chem.* **2005**, *178*, 1575-1579.

(40) Belik, A. A. *J. Solid State Chem.* **2012**, *195*, 32-40.

(41) Jiang, N.; Spence, J. C. H. J. Phys.: Condens. Matter **2006**, *18*, 8029-8036.

(42) Hu, Z.; von Lips, H.; Golden, M. S.; Fink, J.; Kaindl, G.; De Groot, F. M. F.; Ebbinghaus, S.; Reller, A. *Phys. Rev. B* **2000**, *61*, 5262-5266.

(43) Liu, R. S.; Jang, L. Y.; Hung, H. H.; Tallon, J. L. *Phys. Rev. B* **2001**, *63*, 212507.

(44) Newville, M. "Fundamentals in XAFS," Consortium for Advanced Radiation Sources, University of Chicago: Chicago, 2004.

(45) Mugavero III, S. J.; Smith, M. D.; Yoon, W. S.; Zur, Loye, H. C. *Angew. Chem. Int. Ed.* **2009**. *48*, 215-218.

(46) Di Salvo, F.; Escola, N.; Scherlis, D. A.; Estrin, D. A.; Bondia, C.; Murgida, D.; Ramallo- López, J. M.; Requejo, F. G.; Shimon, L.; Doctorovich, F. *Chem. Eur. J* **2007**, *13*, 8428-8436.

(47) Lee, C. H.; Oyanagi, H.; Sekine, C.; Shirotani, I.; Ishii. M. *Phys. Rev. B,* **1999**, *60*, 13253-13256

(48) Zhang, Z.; Kennedy, B. J.; Howard, C. J.; Jang, L. Y.; Knight, K. S.; Matsuda, M.; Miyake, M. *J. Phys.: Condens. Matter*, **2010**, *22*, 445401.

(49) Le Fevre, P.; Magnan, H.; Chandesris, D.; Vogel, J.; Formoso, V.; Comin, F. *Phys. Rev. B,* **1998***, 58*, 1080-1083.

(50) Kotani, A.; Kvashnina, K. O.; Glatzel, P.; Kvashnina, J. C.; Glatzel, P. *Phys. Rev. B* **2012**, *108*, 036403.

(51) Nachimuthu, P.; Shih, W. C.; Liu, R. S.; Jang, L. Y.; Chen J.- M. *J. Solid State Chem.*, **2000**, *149*, 408-413.

(52) Purans, J.; Azens, A.; Granqvist, C. G. *Electrochimica. Acta.* **2001**, *46*, 2055-2058.

(53) Zhou, Q.; Blanchard, P. E. R.; Kennedy, B. J.; Reynolds, E.; Zhang, Z.; Miiler, W.; Aitken, J. B.; Avdeev, M.; Jang, L. Y.; Kimpton, J. A. *Chem. Mater.* **2010**, *24*, 2978-2986.

(54) Hamdan, N. M.; Hussain, Z. *Supercond. Sci. Technol.* **2009**, *22*, 034007.

(55) Bondino, F.; Magnano, E.; Booth, C. H.; Offi, F.; Panaccione, G.; Malvestuto, M.; Paolicelli, G.; Simonelli, L. F.; Parmigiani, F.; McGuire, M. A.; Sefat, A. S.; Sales, B. C.; Jin, R.; Vilmercati, P.; Mandrus, D.; Singh, D. J.; Mannella, N. *Phys. Rev. B* **2010**, *82*, 014529.

(56) Wang, R.; Fang, M. *J. Mater. Chem.* **2012**, *22*, 1770-1773.

(57) Huynh, L. T.; Eger, S. B.; Walker, J. D. S.; Hayes, J. R.; Gaultois, M. W.; Grosvenor, A. P. *Solid State Sci.* **2012**, *14*, 761-767.

Figure Captions

Figure 1. Variation in unit cell volumes (blue squares) and monoclinic angle β (red circles) at room temperature across the (a) $Ba_3La_{1-x}Bi_xIr_2O_9$, (b) $Ba_3La_{1-x}Bi_xRu_2O_9$, (c) $Ba_3Ce_{1-x}Bi_xRu_2O_9$ and (d) $Ba_3La_{1-x}Ce_xIr_2O_9$ solid solutions. Data were obtained by Rietveld-refinement against S-XRD data, except for the value of $Ba_3CeRu_2O_9$ which is taken from Ref (10).

Figure 2. Unit cell volumes of (a) $Ba_3La_{1-x}Bi_xIr_2O_9$, (b) $Ba_3La_{1-x}Bi_xRu_2O_9$ and (c) $Ba_3Ce_{1-x}Bi_xRu_2O_9$ as a function of temperature through the magnetovolume transitions at the Bi-rich ends of the solid-solutions. Data were obtained by Rietveld-refinement against NPD ($Ba_3La_{1-x}Bi_xIr_2O_9$), S-XRD ($Ba_3La_{1-x}Bi_xRu_2O_9$) and conventional XRD ($Ba_3Ce_{1-x}Bi_xRu_2O_9$) data.

Figure 3. Magnetic susceptibility as a function of temperature for (a) $Ba_3La_{1-x}Bi_xIr_2O_9$ (b) $Ba_3La_{1-x}Bi_xRu_2O_9$ and (c) $Ba_3Ce_{1-x}Bi_xRu_2O_9$.

Figure 4. Normalized Bi L_3-edge XANES spectra of $Ba_3BiRu_2O_9$, Bi_2O_3, Ba_2LuBiO_6, and $BaBiO_3$. All spectra were collected in fluorescence mode.

Figure 5. Normalized (upper) and first derivative (lower) Ru L_3-edge XANES spectra of a) $Ba_3\mathit{B}Ru_2O_9$ (B = La, Ce, Bi) and b) standards $SrRuO_3$ (Ru^{4+}) and Sr_2YRuO_6 (Ru^{5+}). All spectra were presented in TEY mode.

Figure 6. Representative normalized Ru L_3-edge XANES spectra of a) $Ba_3La_{1-x}Ce_xRu_2O_9$, b), $Ba_3Ce_{1-x}Bi_xRu_2O_9$ and c) $Ba_3La_{1-x}Bi_xRu_2O_9$. All spectra were presented in TEY mode.

Figure 7. Plots of the Ru L_3-edge absorption edge energy as a function of x for $Ba_3La_{1-x}Ce_xRu_2O_9$, $Ba_3Ce_{1-x}Bi_xRu_2O_9$ and $Ba_3La_{1-x}Bi_xRu_2O_9$.

Figure 8. a) The Ru L_3-edge XANES spectrum of $Ba_3BiRu_2O_9$, including the corresponding fit and individual components ($Ba_3LaRu_2O_9$ and $Ba_3CeRu_2O_9$). b) Ru oxidation states as a

function of x in $Ba_3La_{1-x}Ce_xRu_2O_9$, $Ba_3Ce_{1-x}Bi_xRu_2O_9$, and $Ba_3La_{1-x}Bi_xRu_2O_9$. All oxidation states were estimated from linear combination fitting analysis of the Ru L_3-edge XANES spectra.

Figure 9. a) Normalized Ir L_3-edge XANES spectra of $Ba_3La_{1-x}Bi_xIr_2O_9$. Inset compares the edge onset for $Ba_3LaIr_2O_9$ and $Ba_3BiIr_2O_9$. b) The first derivative Ir L_3-edge XANES spectra of $Ba_3LaIr_2O_9$ (black) and $Ba_3BiIr_2O_9$. Dashed lines represents the Ir L_3-edge absorption edge energies. c) The Ir L_3-edge integrated intensities, normalized to the integrated intensity of $Ba_3LaIr_2O_9$. All spectra were presented in fluorescence mode.

Figure 10. Representative normalized Ce L_3-edge XANES spectra of a) Ce standards compared to $Ba_3CeRu_2O_9$, b) $Ba_3La_{1-x}Ce_xRu_2O_9$, and c) $Ba_3Ce_{1-x}Bi_xRu_2O_9$. Spectra were collected for Ce-rich samples because of overlap with the Ba L_2-edge. All spectra were presented in fluorescence mode.

Figure 11. Representative normalized Ce $M_{5,4}$-edge XANES spectra of a) Ce standards compared to $Ba_3CeRu_2O_9$, b) $Ba_3La_{1-x}Ce_xRu_2O_9$, and c) $Ba_3Ce_{1-x}Bi_xRu_2O_9$. Peaks corresponding to Ce^{3+} and Ce^{4+} are marked as △ and *, respectively. All spectra were presented in TEY mode.

Figure 1

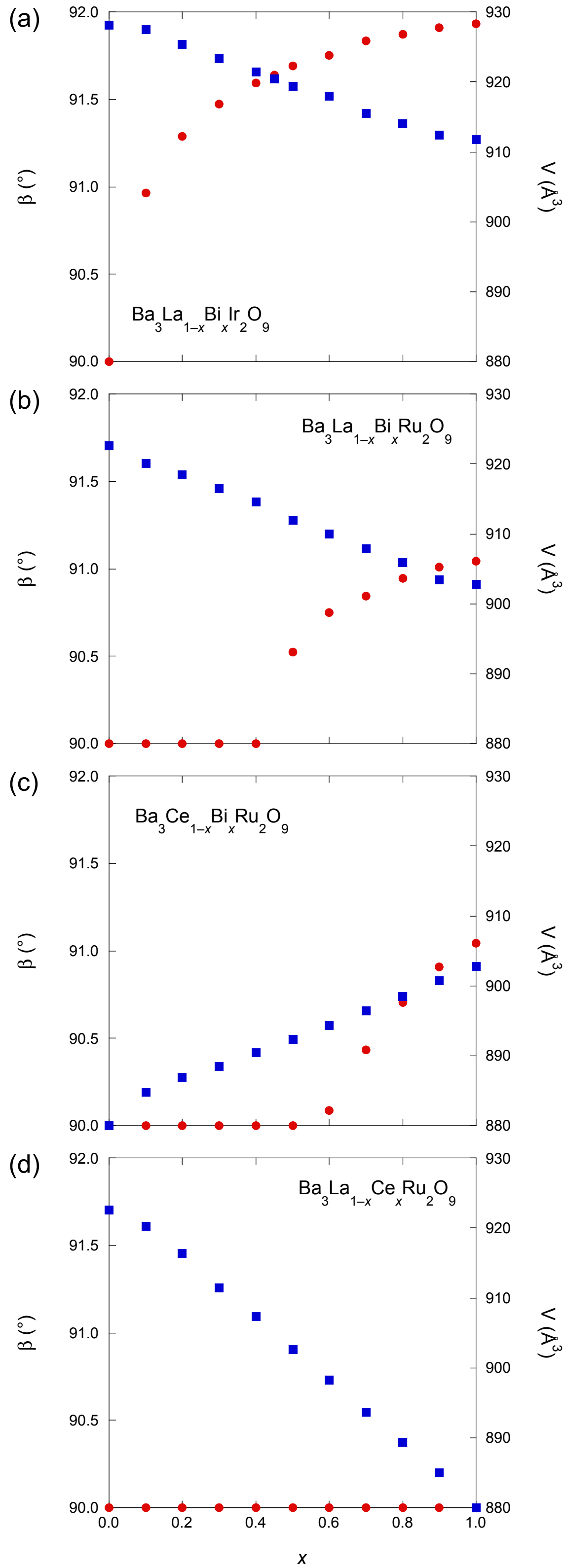
(a)
(b)
(c)
(d)
Ba3La1−xBixIr2O9
Ba3La1−xBixRu2O9
Ba3Ce1−xBixRu2O9
Ba3La1−xCexRu2O9
β (°)
V (Å3)
92.0
91.5
91.0
90.5
90.0
930
920
910
900
890
880
0.0
0.2
0.4
0.6
0.8
1.0
x

Figure 2

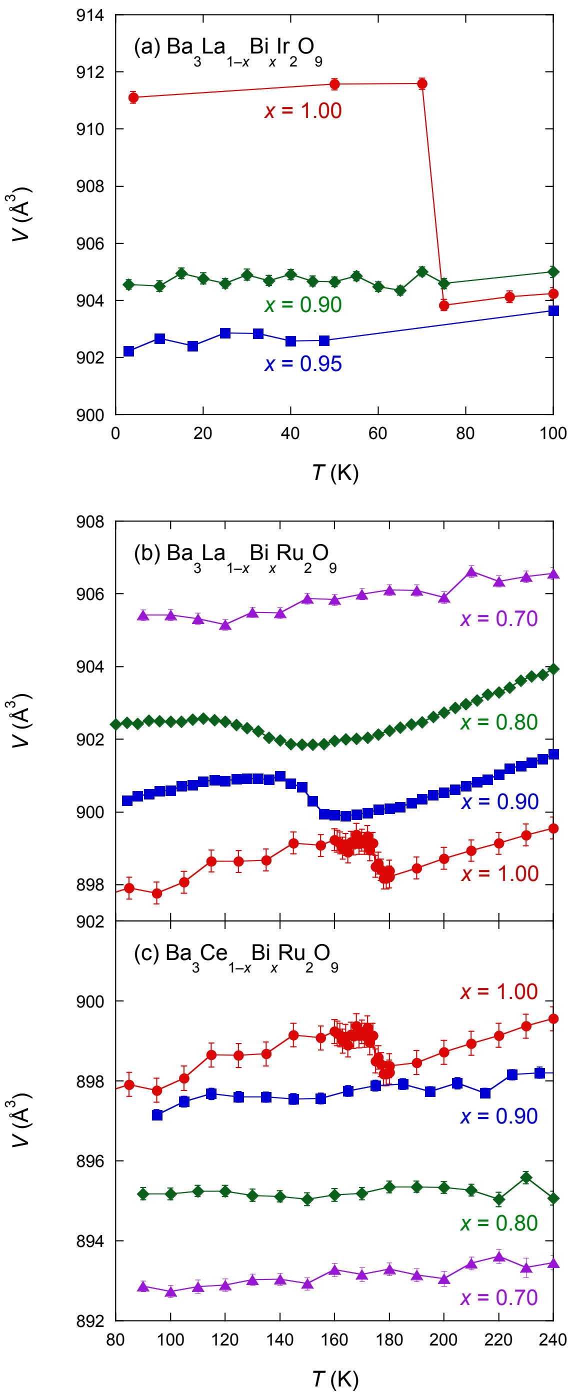

(a) Ba3La1−xBixIr2O9
x = 1.00
x = 0.90
x = 0.95
V (Å3)
T (K)
(b) Ba3La1−xBixRu2O9
x = 0.70
x = 0.80
x = 0.90
x = 1.00
V (Å3)
(c) Ba3Ce1−xBixRu2O9
x = 1.00
x = 0.90
x = 0.80
x = 0.70
V (Å3)
T (K)

Figure 3

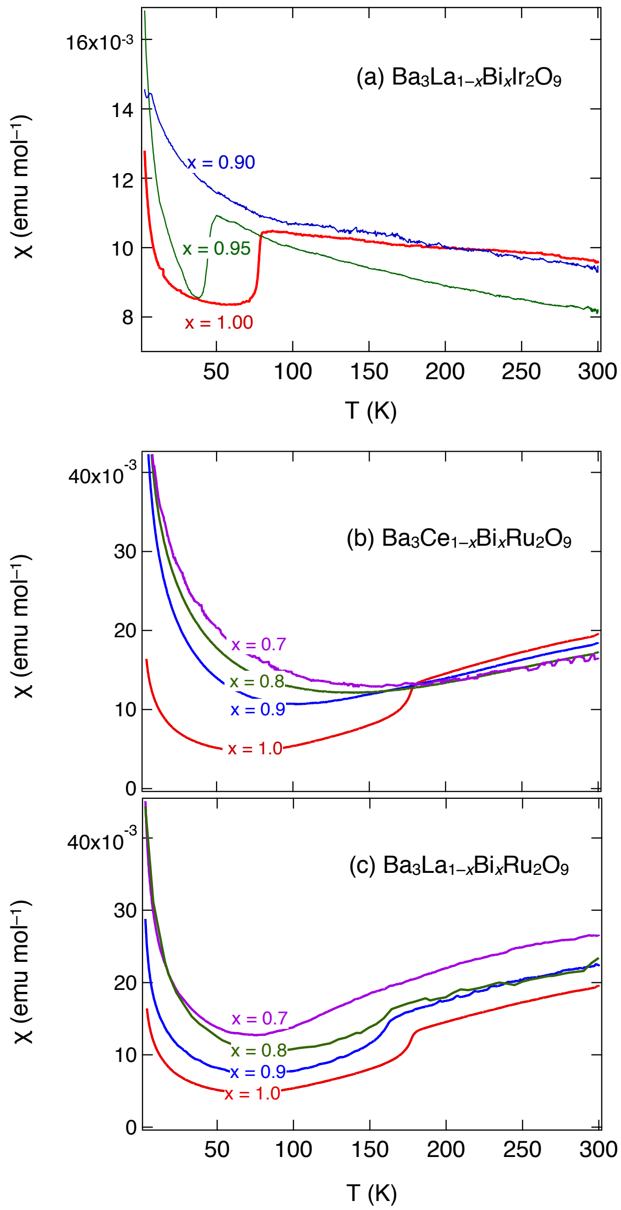

(a) Ba3La1−xBixIr2O9
x = 0.90
x = 0.95
x = 1.00
χ (emu mol−1)
16x10-3
14
12
10
8
50
100
150
200
250
300
T (K)
(b) Ba3Ce1−xBixRu2O9
x = 0.7
x = 0.8
x = 0.9
x = 1.0
40x10-3
30
20
10
0
(c) Ba3La1−xBixRu2O9
x = 0.7
x = 0.8
x = 0.9
x = 1.0

Figure 4

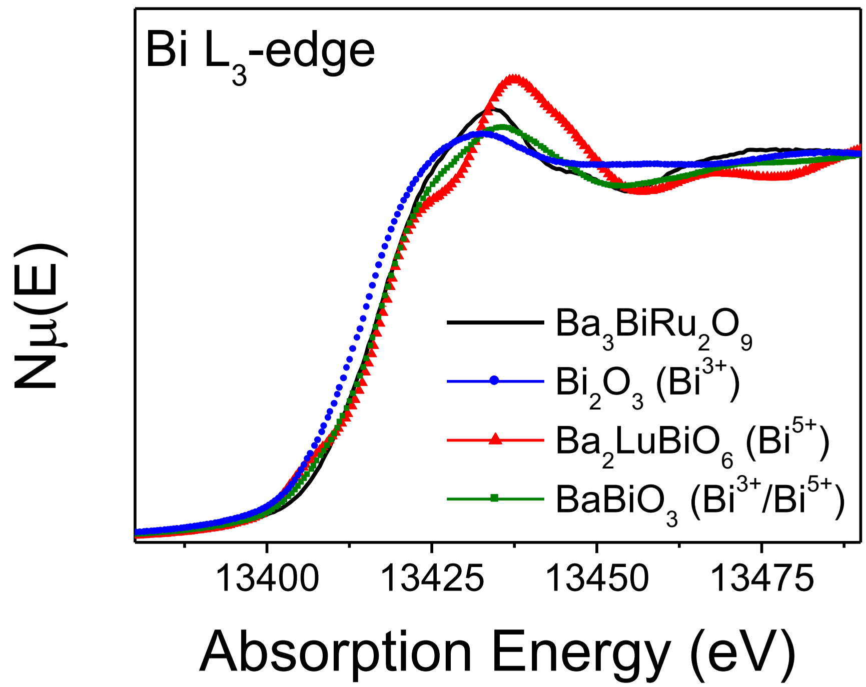
Bi L3-edge
Nμ(E)
Ba3BiRu2O9
Bi2O3 (Bi3+)
Ba2LuBiO6 (Bi5+)
BaBiO3 (Bi3+/Bi5+)
13400
13425
13450
13475
Absorption Energy (eV)

Figure 5

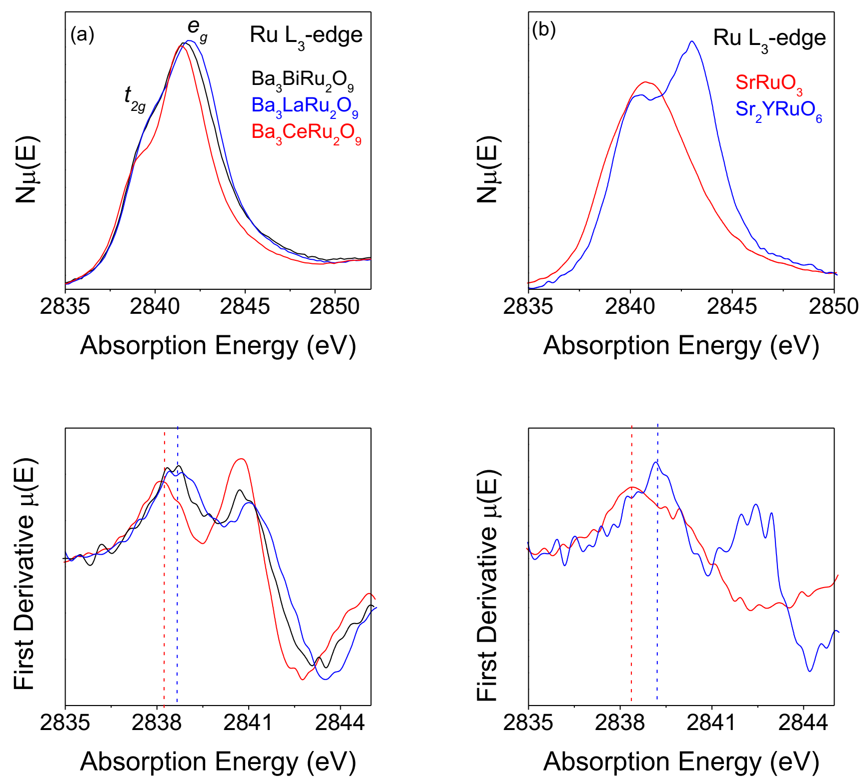

(a)
Ru L3-edge
eg
t2g
Ba3BiRu2O9
Ba3LaRu2O9
Ba3CeRu2O9
Nμ(E)
2835
2840
2845
2850
Absorption Energy (eV)
(b)
Ru L3-edge
SrRuO3
Sr2YRuO6
Nμ(E)
2835
2840
2845
2850
Absorption Energy (eV)
First Derivative μ(E)
2835
2838
2841
2844
Absorption Energy (eV)
First Derivative μ(E)
2835
2838
2841
2844
Absorption Energy (eV)

Figure 6

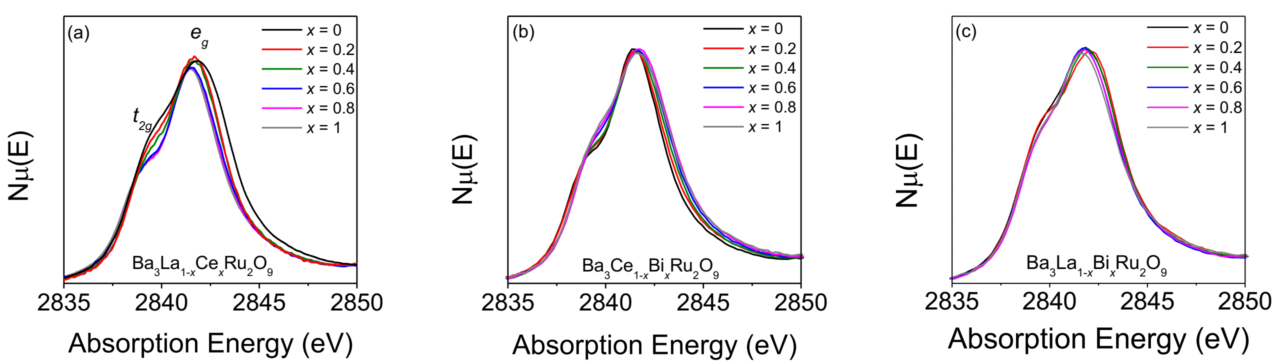

(a)
e_g
t_{2g}
x = 0
x = 0.2
x = 0.4
x = 0.6
x = 0.8
x = 1
Nμ(E)
$Ba_3La_{1-x}Ce_xRu_2O_9$
2835
2840
2845
2850
Absorption Energy (eV)
(b)
x = 0
x = 0.2
x = 0.4
x = 0.6
x = 0.8
x = 1
Nμ(E)
$Ba_3Ce_{1-x}Bi_xRu_2O_9$
2835
2840
2845
2850
Absorption Energy (eV)
(c)
x = 0
x = 0.2
x = 0.4
x = 0.6
x = 0.8
x = 1
Nμ(E)
$Ba_3La_{1-x}Bi_xRu_2O_9$
2835
2840
2845
2850
Absorption Energy (eV)

Figure 7

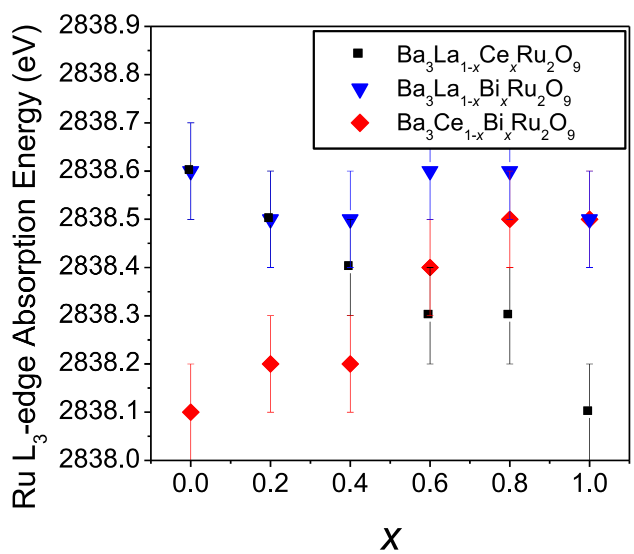

Ru L3-edge Absorption Energy (eV)
2838.9
2838.8
2838.7
2838.6
2838.5
2838.4
2838.3
2838.2
2838.1
2838.0
0.0
0.2
0.4
0.6
0.8
1.0
x
Ba3La1-xCexRu2O9
Ba3La1-xBixRu2O9
Ba3Ce1-xBixRu2O9

Figure 8

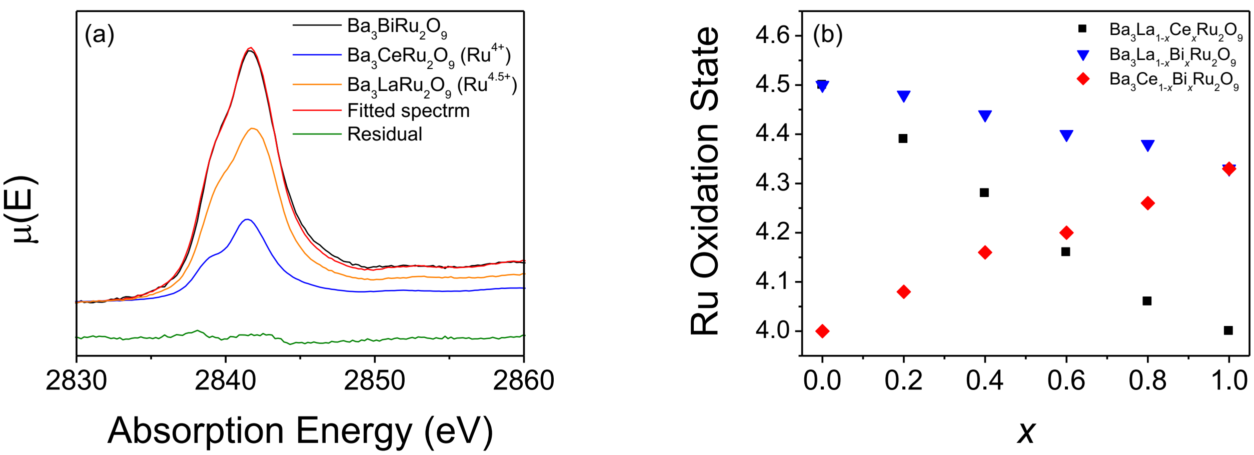
(a)
Ba3BiRu2O9
Ba3CeRu2O9 (Ru4+)
Ba3LaRu2O9 (Ru4.5+)
Fitted spectrm
Residual
μ(E)
2830
2840
2850
2860
Absorption Energy (eV)
(b)
Ba3La1-xCexRu2O9
Ba3La1-xBixRu2O9
Ba3Ce1-xBixRu2O9
Ru Oxidation State
4.0
4.1
4.2
4.3
4.4
4.5
4.6
0.0
0.2
0.4
0.6
0.8
1.0
x

Figure 9

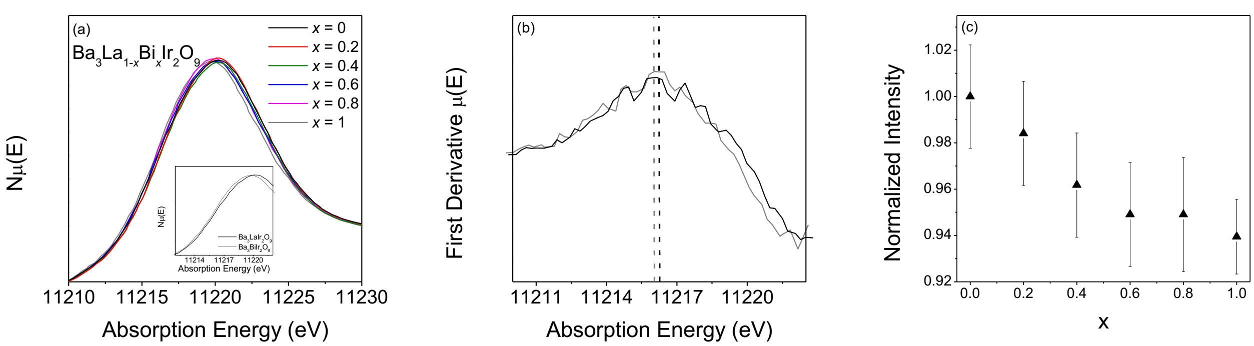

(a)
Ba3La1-xBixIr2O9
x = 0
x = 0.2
x = 0.4
x = 0.6
x = 0.8
x = 1
Nμ(E)
11210
11215
11220
11225
11230
Absorption Energy (eV)
(b)
First Derivative μ(E)
11211
11214
11217
11220
Absorption Energy (eV)
(c)
Normalized Intensity
1.02
1.00
0.98
0.96
0.94
0.92
0.0
0.2
0.4
0.6
0.8
1.0
x

Figure 10

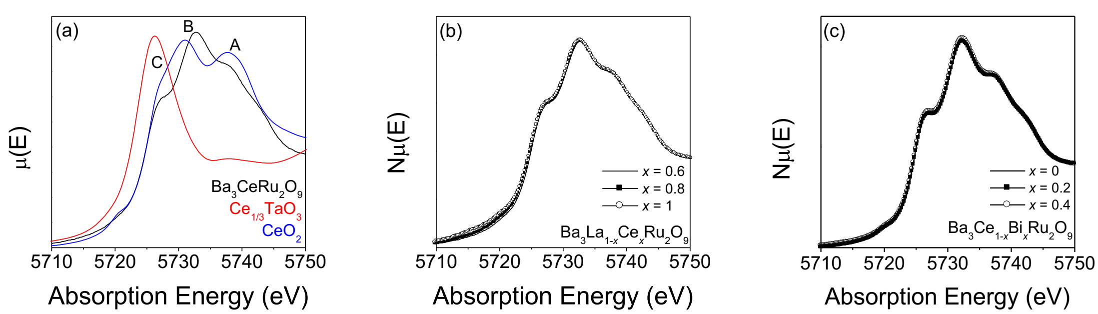

(a)
B
A
C
μ(E)
Ba3CeRu2O9
Ce1/3TaO3
CeO2
5710 5720 5730 5740 5750
Absorption Energy (eV)
(b)
Nμ(E)
x = 0.6
x = 0.8
x = 1
Ba3La1-xCexRu2O9
5710 5720 5730 5740 5750
Absorption Energy (eV)
(c)
Nμ(E)
x = 0
x = 0.2
x = 0.4
Ba3Ce1-xBixRu2O9
5710 5720 5730 5740 5750
Absorption Energy (eV)

Figure 11

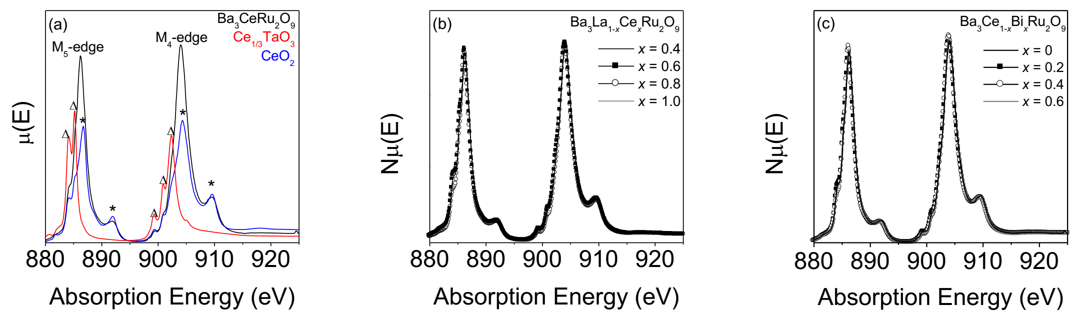

(a)
Ba3CeRu2O9
Ce1/3TaO3
CeO2
M5-edge
M4-edge
μ(E)
880 890 900 910 920
Absorption Energy (eV)
(b)
Ba3La1-xCexRu2O9
x = 0.4
x = 0.6
x = 0.8
x = 1.0
Nμ(E)
880 890 900 910 920
Absorption Energy (eV)
(c)
Ba3Ce1-xBixRu2O9
x = 0
x = 0.2
x = 0.4
x = 0.6
Nμ(E)
880 890 900 910 920
Absorption Energy (eV)

Table of Contents Figure

Magnetic susceptibility as a function of temperature for $Ba_3La_{1-x}Bi_xIr_2O_9$, showing suppression of the magnetic ordering with doping of the Bi site.